



Article

How Representative Are European AERONET-OC Sites of European Marine Waters?

Ilaria Cazzaniga * and Frédéric Mélin

Joint Research Centre (JRC), European Commission, 21027 Ispra, Italy; frederic.melin@ec.europa.eu

* Correspondence: ilaria.cazzaniga@ec.europa.eu

Abstract: Data from the Ocean Color component of the Aerosol Robotic Network (AERONET-OC) have been extensively used to assess Ocean Color radiometric products from various satellite sensors. This study, focusing on Ocean Color radiometric operational products from the Sentinel-3 Ocean and Land Colour Instrument (OLCI), aims at investigating where in the European seas the results of match-up analyses at the European marine AERONET-OC sites could be applicable. Data clustering is applied to OLCI remote sensing reflectance $R_{RS}(\lambda)$ from the various sites to define different sets of optical classes, which are later used to identify class-based uncertainties. A set of fifteen classes grants medium-to-high classification levels to most European seas, with exceptions in the South-East Mediterranean Sea, the Atlantic Ocean, or the Gulf of Bothnia. In these areas, $R_{RS}(\lambda)$ spectra are very often identified as novel with respect to the generated set of classes, suggesting their under-representation in AERONET-OC data. Uncertainties are finally mapped onto European seas according to class membership. The largest uncertainty values are obtained in the blue spectral region for almost all classes. In clear waters, larger values are obtained in the blue bands. Conversely, larger values are shown in the green and red bands in coastal and turbid waters.

Keywords: optical water types; remote sensing reflectance; AERONET-OC; classification; ocean color; OLCI; validation



Citation: Cazzaniga, I.; Mélin, F. How Representative Are European AERONET-OC Sites of European Marine Waters? *Remote Sens.* **2024**, *16*, 1793. <https://doi.org/10.3390/rs16101793>

Academic Editors: Peng Chen and Jason Keith Jolliff

Received: 25 March 2024

Revised: 14 May 2024

Accepted: 16 May 2024

Published: 18 May 2024



Copyright: © 2024 by the authors. Licensee MDPI, Basel, Switzerland. This article is an open access article distributed under the terms and conditions of the Creative Commons Attribution (CC BY) license (<https://creativecommons.org/licenses/by/4.0/>).

1. Introduction

The quantification of the accuracy of satellite-derived normalized water leaving radiance ($L_{WN}(\lambda)$) or remote sensing reflectance ($R_{RS}(\lambda)$) is the matter of extensive validation programs. The Ocean Color component of the Aerosol Robotic Network (AERONET-OC) was conceived to support the assessment of satellite radiometric products, with automated radiometers providing values of $L_{WN}(\lambda)$ in a variety of water types [1,2]. In the European seas, nine sites have produced a substantial amount of data in coastal areas (Figure 1). They are generally considered representative of:

- Case 1 waters, with the Casablanca (CSP) site in the Western Mediterranean Sea;
- Optically complex waters with varying concentrations of sediments and chromophoric dissolved organic matter (CDOM) with the Acqua Alta Oceanographic Tower site (AAOT) in the northern Adriatic Sea, the Galata Platform (GLT), and the Section-7 Platform (ST7) sites in the Black Sea and the Thornton-C-Power (TCP) site off the Belgian coast [3];
- Optically complex waters with high concentrations of CDOM, with the Gustaf Dalén Lighthouse Tower (GDLT), the Helsinki Lighthouse (HLT), and the Irbe Lighthouse (IRLT) sites in the Baltic Sea;
- Highly turbid waters with the Zeebrugge-MOW (ZEE) site in nearshore waters off the Belgian coast [4].

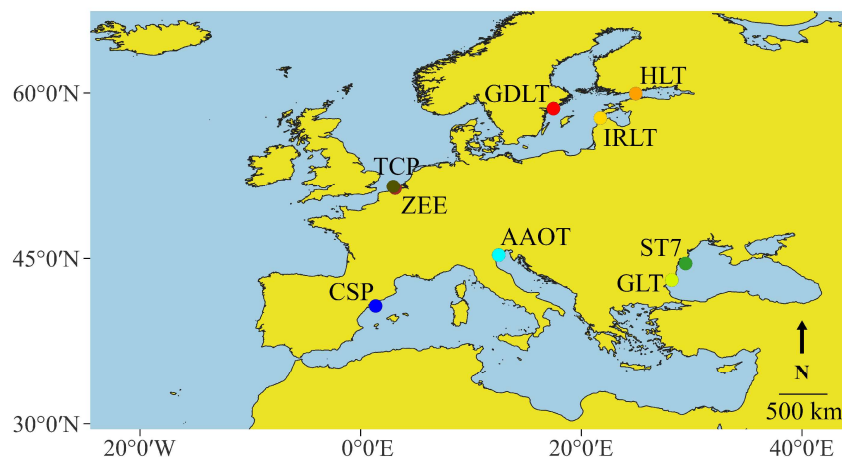


Figure 1. Location of the European AERONET-OC marine sites.

Therefore, the European AERONET-OC sites cover a significant range of natural optical variability, and several works benefit from their data to assess the uncertainties of various Ocean Color radiometric products derived from various satellite-borne sensors. In fact, most validation data used for some European seas from a variety of missions are coming from AERONET-OC [5–9]. The results of these analyses are often presented site by site (e.g., [5,7,10–12]), with sites grouped by regions [13–15] or by water types as listed above (e.g., [6,9,16]). Among other sensors, Ocean Color products from the Copernicus Sentinel-3A and Sentinel-3B (S3A and S3B) Ocean and Land Colour Instrument (OLCI) have also been assessed with AERONET-OC data by, e.g., [6,14,16–21].

This study aims at investigating where in the European seas the results of match-up analyses between OLCI and AERONET-OC data at these sites could be applicable, besides the area close to the AERONET-OC sites themselves. It relies on a framework of optical clustering and classification under the assumption that uncertainty estimates are similar for similar optical water types (OWTs) [11,22–26]. In [27], Moore and colleagues assessed SeaWiFS and MODIS-Aqua $R_{RS}(\lambda)$ uncertainty metrics based on OWTs, showing a dependence on water types. Jackson and colleagues [25] used this framework to provide per-pixel uncertainty values for Ocean Colour Climate Change Initiative (OC-CCI) products. Liu and colleagues [26] finally relied on it to provide per-pixel uncertainty estimates for MERIS-derived chlorophyll-a products. Additionally, optical water classes were used to provide a class-based performance of $R_{RS}(\lambda)$ or $L_{WN}(\lambda)$ products derived through various atmospheric correction algorithms by, e.g., [11,28,29]. This framework is indeed supported by the observation that validation statistics significantly vary across sites generally associated with different water types (e.g., [12]); in the specific case of OLCI radiometric products, a clear dependence of validation results on water type and optical complexity was demonstrated in [6].

In this work, $R_{RS}(\lambda)$ values over AERONET-OC sites were first used to define a classification scheme. This classification scheme was later used to verify to what extent the rest of the European sea waters can be classified through optical classes encountered at the AERONET-OC sites. As a second step, this classification scheme was applied to map validation statistics results associated with OLCI $R_{RS}(\lambda)$ radiometric products at European AERONET-OC sites over all European seas.

2. Materials and Methods

2.1. AERONET-OC Data

$L_{WN}(\lambda)$ data were obtained from the various European AERONET-OC marine sites. Only data from the latest years were considered: starting from 2017, in fact, new radiometers (CE318T) were deployed at the various sites [2]. These instruments provide $L_{WN}(\lambda)$ at 11 center-wavelengths almost overlapping most OLCI bands, reducing the uncertainties

that could be introduced by the use of band-shifting techniques when comparing field and satellite data [30,31].

For all sites, in situ $R_{RS}(\lambda)$ were obtained from Level 2 quality-checked $L_{WN}(\lambda)$ data corrected for bidirectional (*BRDF*) effects, following [32] (which is a standard AERONET-OC radiometric product), according to Equation (1):

$$R_{RS}(\lambda) = \frac{L_{WN}(\lambda)}{F_0(\lambda)} \quad (1)$$

where $F_0(\lambda)$ is the mean spectral extra-atmospheric irradiance from [33]. Clustering was applied to in situ data after normalizing $R_{RS}(\lambda)$ by its spectrally integrated value to obtain a normalized $R_{RS}(\lambda)$, i.e., $nR_{RS}(\lambda)$, as in Equation (2):

$$nR_{RS}(\lambda) = \frac{R_{RS}(\lambda)}{\int_{\lambda_1}^{\lambda_2} R_{RS}(\lambda) d\lambda} \quad (2)$$

where $\lambda_1 = 412.5$ nm and $\lambda_2 = 665$ nm. Clustering and consequently classification thus focused on the spectral shape rather than the amplitude of $R_{RS}(\lambda)$ [34,35]. Finally, more than 37,000 spectra were included in the cluster analysis.

2.2. Satellite Data

Clustering was also applied to satellite OLCI data. Level 2 Ocean Color products (reduced resolution RR, Collection 3 [36]) from both S3A and S3B satellites were obtained from the Data Centre of the European Organisation for the Exploitation of Meteorological Satellites (EUMETSAT). OLCI $R_{RS}(\lambda)$ values were derived from standard atmospherically corrected reflectance products, corrected for *BRDF* effects following [32] and excluding unreliable pixel values applying the recommended flags [36]. Since slightly negative values are accepted by quality flags, in order to avoid handling negative values in the clustering, an offset of 0.00185 sr^{-1} was applied to $R_{RS}(\lambda)$ data. This value is the largest negative value (divided by π) admitted by exclusion flags for reflectance in the 412.5–665-nm range in OLCI products (as in the *OL_2_ACP_AX* Auxiliary data file). Note that this same offset was applied to AERONET-OC data before normalization as well, for consistency.

$R_{RS}(\lambda)$ values were obtained over each AERONET-OC site, extracting all the pixels in a 3×3 window centered at the site location, from April 2016 to March 2023. Extracted data were excluded whenever any of the 9-pixel values was flagged to reduce the risk of cloud contamination. Some pixels passed quality flag filtering even when showing unrealistic spectral shapes typical of ‘clear waters’ at the Baltic, North, and Black Sea sites, which are never encountered in in situ time series. These pixels were thus excluded before clustering, discarding the whole spectrum when $R_{RS}(490) < R_{RS}(412)$ in the Black Sea or $R_{RS}(510) < R_{RS}(412)$ in the Baltic Sea. Finally, about 61’000 spectra were included in the cluster analysis.

AERONET-OC and OLCI match-ups were built for both S3A and S3B data using extracted data at each site, as in [7]. Data from the older model of radiometers (CE318) were considered, and $L_{WN}(\lambda)$ values were band-shifted to corresponding S3-OLCI center-wavelengths, following [30], only for the ZEE and TCP sites, where only CE318-type instruments were deployed.

Finally, the whole 2022 S3-OLCI time series over Europe (min/max longitude: 24.5°W , 44.7°E ; min/max latitude: 29.5°N , 67.4°N) was instead used to apply the classification schemes at the scale of the European seas. In this second step, OLCI products were binned into a regular grid with a sinusoidal projection with cells of 1×1 km at the Equator, i.e., 0.008 deg. This facilitated the calculation of classification statistics on a regular grid. The same offset of 0.00185 sr^{-1} and normalization were also applied before classification.

2.3. Data Clustering

Clustering was first applied to in situ data considering all available $R_{RS}(\lambda)$ spectra at center-wavelengths between 412.5 and 665 nm for the overlapping OLCI and AERONET-OC center-wavelengths [2]. The 400 nm band, for which the highest uncertainties have been reported for OLCI [6], and the near-infrared bands, considering the large uncertainties affecting AERONET-OC $R_{RS}(\lambda)$ in this spectral region, were excluded [2,6]. At this stage, ZEE and TCP data were also excluded to avoid introducing unpredictable uncertainties due to band shifting. The set of classes generated by clustering in situ data is hereafter referred to as ‘in situ’ set.

Secondly, a cluster analysis was performed with satellite-derived spectra over all European sites in two different configurations. In the first one, AERONET-OC sites were considered individually, and a set of clusters was created for each site. In fact, since validation results have been usually presented per site or group of sites, this configuration was useful in identifying where validation results for the various AERONET-OC sites could be directly extended in the European seas. The sets of classes derived from this configuration are hereafter indicated as the ‘OLCI-XX’ sets, where XX is meant to be replaced by the name of the various sites. In a second configuration, all the spectra from all the sites were considered as a bulk, and a single set of classes was generated. This second configuration was used in the second part of the analysis, i.e., to estimate class-based validation statistics and to characterize their distribution in the European sea waters. The set of classes derived in this second configuration is hereafter identified with ‘OLCI-all’ set.

As in [34], an ISODATA unsupervised classification algorithm (the Iterative Self-Organizing Data Analysis Technique [37]), as implemented in the ENVI 5.7 software (ISODATA, 2023, <https://www.13harrisgeospatial.com/docs/ISODATAClassification.html>), was applied for data clustering to generate optical water classes. ISODATA differs from other k -means clustering algorithms, since it automatically adjusts the number of clusters during the clustering iterative process. Each cluster is in fact split whenever its spectral standard deviation exceeds a predefined threshold iso_{std} , whereas clusters are merged whenever their distance is below a given threshold iso_d . These two parameters, iso_{std} and iso_d , still need to be defined by the user. Additional parameters of ISODATA are the target number of clusters and the maximum number of cluster pairs that can be merged at each iteration. The choice of all these parameters, which is quite arbitrary but strictly depends on the number of bands associated with the input data and on the input data itself, is discussed later in this manuscript.

2.4. European Sea Water Classification

For each set of clusters, classes were defined by mean spectral values μ_c and related covariance matrix Σ_c^2 for each class c from the population assigned to each cluster, as conducted in previous works, e.g., [22,25,34]. To relate a given spectral $R_{RS}(\lambda)$ value i to a class c , its class membership value $p(c, i)$ was calculated according to the following:

$$p(c, i) = 1 - P\left(\Delta_c^2(i), n\right) \quad (3)$$

where P is the cumulative χ^2 distribution function with n degrees of freedom [38] of the Mahalanobis distance Δ_c^2 :

$$\Delta_c^2(i) = (i - \mu_c)^T \Sigma_c^{-2} (i - \mu_c) \quad (4)$$

The class showing the highest class membership was then assigned to the spectral value i . The total membership $p_t(i)$ was calculated as follows:

$$p_t(i) = \sum_{c=1}^N p(c, i) \quad (5)$$

Spectra with a maximum class membership close to nil (in practice, lower than 10^{-8} , as in [29]) were considered unclassified, and class 0 was assigned. For these spectra, $p_t(i)$ was set to 0.

The ‘in situ’ set of classes was first used to classify matching (i.e., quasi-synchronous data pairs) OLCI and AERONET-OC spectra in order to evaluate the coherence of their respective classification. Considering the high rate of misclassification obtained when classifying OLCI spectra with the ‘in situ’ set (see Section 3) and that OLCI-derived $R_{RS}(\lambda)$ spectra are ultimately the data that need to be classified, OLCI-derived sets of classes were used to complete the following steps of this work.

Both the ‘OLCI-XX’ set and the ‘OLCI-all’ set were thus used to classify the $nR_{RS}(\lambda)$ spectra from the 2022 time series of OLCI binned data over the European seas. Mean class membership and mean total membership values were calculated over the bin, and a class was assigned to each bin and each day. The frequency of occurrence of each class for each bin was also calculated for the whole year. When using the various ‘OLCI-XX’ sets, the classification was repeated for each set of classes, i.e., for each site. For each bin and day, the site for which the largest class membership was obtained was considered the most representative. Class membership was preferred to the total one to avoid that the number of classes at each site could affect the results.

Finally, in order to detect those areas not well represented by AERONET-OC site OWTs, a novelty detection approach was applied [39,40]. In fact, the total membership in the form expressed here does not have any constraints: it can exceed 1 and the selection of any minimum value of $p_t(i)$, indicating a low or high membership is quite arbitrary. As in [39,40], a spectrum i was considered novel whenever $\Delta_c^2(i)$ from its assigned class c was higher than 12.017, which translates to a $p(c, i)$ of 0.1. In fact, for a given normal multivariate distribution, 90% of the members should show a Δ_c^2 value below a certain threshold, which is 12.017 in the 7-dimensional case [41,42].

2.5. Class-Based Statistics

Aiming at determining the uncertainties related to each class (ideally representing a specific water type), OLCI $R_{RS}(\lambda)$ values were assessed against in situ data for each class. The centered root mean squared difference $RMSD_u(c, \lambda)$ [24] was calculated for each class c at each AERONET-OC center-wavelength λ as follows:

$$RMSD_u(c, \lambda) = \sqrt{RMSD^2(c, \lambda) - \delta^2(c, \lambda)} \quad (6)$$

$$RMSD(c, \lambda) = \sqrt{\frac{\sum_{m=1}^{M_c} p(c, m) \times \left(R_{RS,m}^{insitu}(\lambda) - R_{RS,m}^{OLCI}(\lambda) \right)^2}{\sum_{m=1}^{M_c} p(c, m)}} \quad (7)$$

$$\delta(c, \lambda) = \frac{\sum_{m=1}^M \left(R_{RS,m}^{insitu}(\lambda) - R_{RS,m}^{OLCI}(\lambda) \right) \times p(c, m)}{\sum_{m=1}^{M_c} p(c, m)} \quad (8)$$

Match-ups of in situ and OLCI data were classified using the ‘OLCI-all’ set classification scheme. In total, 1047 and 983 match-ups from S3A and S3B, respectively, were considered. The class membership calculated for the OLCI spectra was generally considered; however, for those spectra showing unrealistic shapes (56 and 58 cases for S3A and S3B, respectively, identified as in Section 2.2), the class and the class membership values of the corresponding in situ spectrum were instead applied to avoid distorting validation statistics. Finally, 7% of the match-ups whose spectra were identified as novel were excluded from match-up statistics calculations.

According to the class statistics definition by [25], $RMSD(c, \lambda)$ and the bias $\delta(c, \lambda)$ were calculated weighting the contribution of match-ups m through the class membership values $p(c, m)$ of each OLCI spectrum, as in Equations (7) and (8), where M is the number of match-ups and $R_{RS,m}^{insitu}(\lambda)$ and $R_{RS,m}^{OLCI}(\lambda)$ are the $R_{RS}(\lambda)$ values of the m -th spectrum from

AERONET-OC and OLCI, respectively. As in [25], $p(c, m)$ values lower than 0.001 were set to 0. The sum of the $p(c, m)$ values within each class represents the effective number of match-ups P_c contributing to each class statistics computation. $RMSD(c, \lambda)$ and $\delta(c, \lambda)$ values were calculated considering S3A and S3B data separately. $RMSD_u(\lambda)$ values were thus calculated for the 2022 OLCI time series, assigning to each bin $R_{RS}(\lambda)$ value i , for each day, a weighted $RMSD_u(i, \lambda)$ value, calculated as follows:

$$RMSD_u(i, \lambda) = \frac{\sum_{c=1}^N p(c, i) \times RMSD_u(c, \lambda)}{p_t(i)} \quad (9)$$

Yearly mean values were finally mapped for S3B and S3A, separately.

3. Results

3.1. ISODATA Parameters

As anticipated, the choice of ISODATA parameters is quite arbitrary. Their choice was a compromise to maximize the mean total membership p_t calculated on the whole clustering dataset and to also avoid p_t values largely above 1, while granting at least a mean p_t value of 0.8 at each site in the satellite data clustering. The total membership was in fact considered medium or high when above 0.3 and 0.8 respectively, as in [29]. iso_d was finally set to 0.0006 and iso_{std} to 0.0015. The target number of clusters was set to 50, largely above the number of clusters expected, to avoid limiting the iterative process. The maximum number of cluster pairs to be merged at each iteration was set to 5. Finally, to avoid the formation of under-represented clusters, a lower limit of 300 spectra per cluster was selected, with the exception of HLT single size configurations, for which a minimum of 150 spectra was set instead. The same parametrization was used for the in situ data clustering.

3.2. Clustering Results

Fourteen clusters were obtained from the in situ data, whose mean $nR_{RS}(\lambda)$ values were used to define the 'in situ' set of classes. From class 1 to class 14 (Figure 2), $nR_{RS}(\lambda)$ mean spectra show their spectral maximum gradually moving from 560 nm for optically complex, CDOM-dominated waters to 490 nm for optically complex waters with varying concentrations of sediments and CDOM and to 412 nm for clear, blue waters. Also, $nR_{RS}(665)$ generally decreases from class 2 to 14. Again, ZEE and TCP, where only CE318-type instruments were deployed, were not included in this cluster analysis to avoid including unknown uncertainties derived from the band-shifting correction needed to align these sites center-wavelengths to those deployed at the other sites.

As anticipated, this set of classes was used to classify the in situ and satellite spectra of 1047 and 983 match-ups from S3A and S3B, respectively. The confusion matrix in Table 1 reports a comparison of the classes of highest memberships obtained for the two types of data and shows that the percentage of misclassified S3A-OLCI spectra (i.e., highest class membership associated with a different class with respect to the field data) often exceeds 50% (from 8% for class 14 to 81% for class 10). This means that differences observed between match-up $R_{RS}(\lambda)$ data (e.g., [6]) are often sufficient to impact the relative class memberships. This being said, the majority of the misclassified spectra are usually assigned to classes adjacent to the correct one. The spectral angle mapper (α) was used to identify spectral similarities among the classes. For each couple of classes j and k , α was calculated as (in radians) follows:

$$\alpha(j, k) = \frac{1}{N_b} \sum_{b=1}^{N_b} \left(\cos^{-1} \left(\frac{\langle \mu_j, \mu_k \rangle}{\|\mu_j\| \|\mu_k\|} \right) \right) \quad (10)$$

where N_b is the number of bands (i.e., 7); $\langle \mu_j, \mu_k \rangle$ is the dot product of class mean spectrum vectors; and $\|\mu_j\|$ and $\|\mu_k\|$ are the Euclidean norms of the same vectors. Considering an arbitrary α value of 5° as a maximum to define ‘adjacent’ classes, the percentage of well-classified spectra raises in all classes. Considering an α value of 10° , more than 90% of the spectra are well classified in all classes. However, since most of the following analysis is focused on classifying OLCI data, OLCI-based clusters are preferred to the ‘in situ’ set.

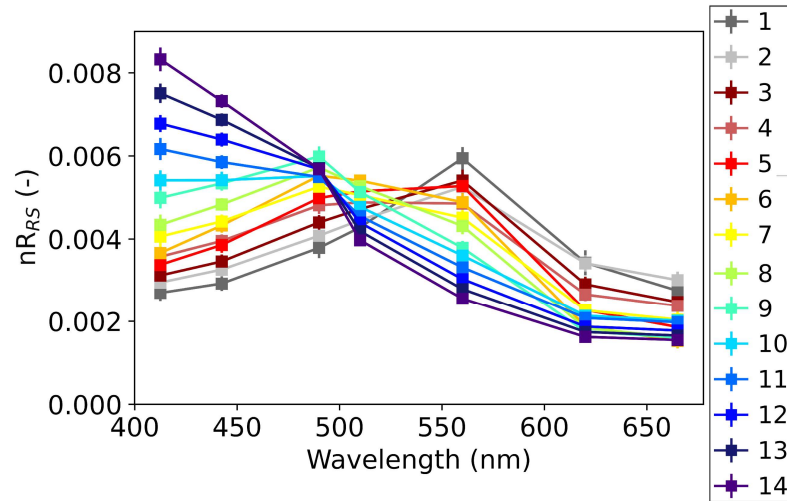


Figure 2. Spectral classes represented by mean and standard deviation (through error bars) values of the fourteen clusters identified by ISODATA from in situ $nR_{RS}(\lambda)$ spectra at the coastal European AERONET-OC sites considered as a bulk (‘in situ’ set).

Table 1. Confusion matrix obtained applying the ‘in situ’ set to S3A and S3B OLCI (along columns) and AERONET-OC (along lines) match-ups ($M = 1819$). % of correctly classified spectra (Correct), % of spectra correctly classified or classified in an adjacent class with $\alpha = 5^\circ$ (α_5) and with $\alpha = 10^\circ$ (α_{10}).

		OLCI Classes														Correct (%)	α_5 (%)	α_{10} (%)	
		1	2	3	4	5	6	7	8	9	10	11	12	13	14				
AERONET-OC classes	1	22	3	9	1	0	0	0	0	0	0	0	0	0	0	0	63	63	97
	2	37	28	23	14	0	0	0	0	0	0	0	0	0	0	0	27	50	100
	3	15	6	48	14	1	0	2	0	0	3	0	0	0	0	0	54	61	94
	4	0	0	13	43	12	0	29	2	0	2	0	0	0	0	0	43	54	98
	5	0	0	7	1	69	10	17	0	0	2	0	0	0	0	0	65	66	98
	6	0	0	0	0	9	46	4	25	6	3	0	0	0	0	0	49	54	90
	7	0	0	0	4	16	6	52	15	3	12	1	0	0	0	0	48	67	99
	8	0	0	0	0	0	10	2	58	20	6	1	0	0	0	0	60	82	99
	9	0	0	0	0	1	0	0	1	21	1	3	0	0	0	0	78	85	96
	10	0	0	0	0	0	0	0	0	1	10	27	14	0	0	0	19	73	100
	11	0	0	0	0	0	0	0	0	0	2	16	17	1	0	0	44	97	100
	12	0	0	0	0	0	0	0	0	0	1	5	22	7	0	0	63	97	100
	13	0	0	0	0	0	0	0	0	0	0	2	4	14	4	0	58	92	100
	14	0	0	0	0	0	0	0	0	0	0	0	2	0	9	0	82	82	100

For OLCI data single sites clustering, the number of clusters varied site by site, as shown by the mean $nR_{RS}(\lambda)$ in Figure 3: they are 4 at IRLT and ZEE, 5 at HLT and TCP, 6 at GDLT, 7 at ST7, 8 at GLT and AAOT, and 9 at CSP, respectively. The ‘OLCI-CSP’ set shows spectra typical of both clear-blue waters and more complex waters, in accordance with the seasonal variability affecting this site. AAOT also shows high variability in terms of spectral shape, which is consistent with a fairly high degree of variability associated with this site (e.g., [43]). The Black Sea sites (GLT and ST7) also show quite high variability in spectral shape. This might be mainly ascribed, on one hand, to the influence of the

coastal run-off (ST7, in particular, is affected by the Danube plume waters [44]), which moves the spectral maximum at 560 nm, and, on the other hand, to the seasonal occurrence of coccolithophores and their coccoliths, which instead tend to move the spectral peak towards the blue spectral region [45,46].

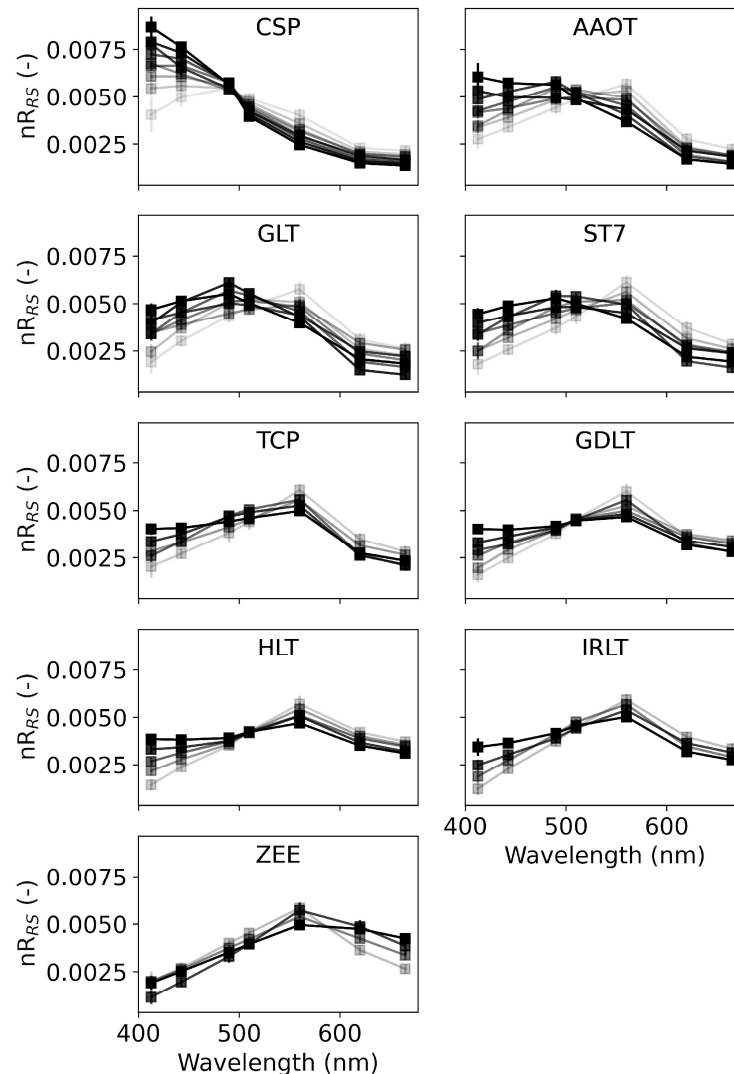


Figure 3. Spectral classes represented by mean and standard deviation values of the clusters identified by ISODATA from OLCI $nR_{RS}(\lambda)$ spectra at each coastal European AERONET-OC site ('OLCI-XX' sets).

Classes from the TCP site have a spectral shape similar to those classes in the Black Sea, showing a spectral maximum at 560 nm. The Baltic Sea sites (GDLT, HLT, and IRLT) show spectra representing absorbing, CDOM-dominated waters, all showing a spectral maximum at 560 nm. Finally, the 'OLCI-ZEE' set shows spectra typical of very turbid waters, with relatively high values in the red, but still with the maximum in the green or a plateau across the green-red region.

Figure 4 shows the results of the cluster analysis run considering all the sites as a bulk, with mean and standard deviation spectral values of $nR_{RS}(\lambda)$ of the fifteen clusters obtained. Considering the relatively high values in the red, classes from 1 to 5 are expected to be representative of more turbid waters, with class 1 also showing the typical spectral shape of highly absorbing waters, i.e., with very low values in the blue.

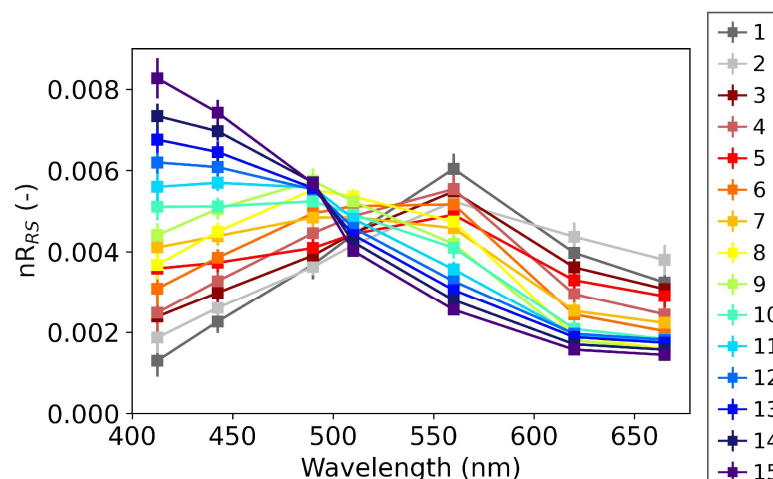


Figure 4. Mean and standard deviation values of the 15 clusters identified by ISODATA from OLCI $nR_{RS}(\lambda)$ spectra at all the coastal European AERONET-OC sites ('OLCI-all' set).

Figure 5 shows the relative contribution of the various sites to each cluster, i.e., in which proportion spectra from the various sites were included in each specific cluster by ISODATA during the cluster analysis. Clusters 1, 3, and 5 are mostly populated by spectra from the Baltic Sea sites, but ZEE, TCP, and ST7 are also included; cluster 2 is instead dominated by ZEE for more than 50%. Cluster 4 is instead mainly populated by spectra from TCP and ST7, this last one being affected by Danube plume CDOM- and sediment-dominated waters [44]. Clusters from 6 to 10, which are representative spectra showing a maximum shifting from 560 nm towards blue bands, are mostly populated by those sites characterized by varying concentrations of sediments and CDOM, i.e., GLT, ST7, TCP, and AAOT. The latter shows an increasing share from 18% in class 7 to 56% in cluster 9. TCP instead disappears after cluster 7, opposite to CSP, whose presence increases. From cluster 11 onward, AAOT and CSP are dominant, with the last 4 clusters showing almost only CSP spectra. Classes from 12 to 15 in fact show a spectral maximum at 412.5 nm, which is typical of clear-blue waters. AAOT contributes to all the 15 clusters (even with 1 spectrum in cluster 2, 5 in cluster 1, and less than 10 in clusters 13 and 14) coherently with the optical variability observed at that site. It is followed by GLT, ST7, and CSP contributing to 11 clusters. Conversely, the Baltic Sea sites and ZEE sites only contributed to 5–7 clusters.

As a complement to Figure 5, Figure 6 summarizes the distribution of the various clusters among the AERONET-OC sites. The most frequent cluster at CSP is 12 (25%), and at AAOT, it is 8 (22%), followed by 9 (20%). In the Black Sea, cluster 7 is prevailing at both sites (26% at GLT and 23% at ST7), followed by cluster 6 (20% and 18%, respectively), showing the marked variability of the water properties at these sites. In the Baltic Sea, cluster 5 is the most frequent (41%) at GDLT, immediately followed by cluster 3 (36%). Clusters 5 and 2 represent both 33% of the HLT spectra. At IRLT, clusters 3 (40%) and 1 (24%) prevail. A total of 35% of the TCP spectra belongs to cluster 4. Finally, at ZEE, 57% of the spectra lay in cluster 2. As expected, Figure 5 graphically confirms the grouping of the AERONET-OC sites into four categories: CSP for Case 1 waters; AAOT, GLT, ST7 and TCP for moderately turbid waters with a fairly large variability, with a higher similarity between AAOT and GLT and between ST7 and TCP; the Baltic sites GDLT, HLT, and IRLT with CDOM-dominated waters; and the ZEE site for turbid sediment-dominated waters.

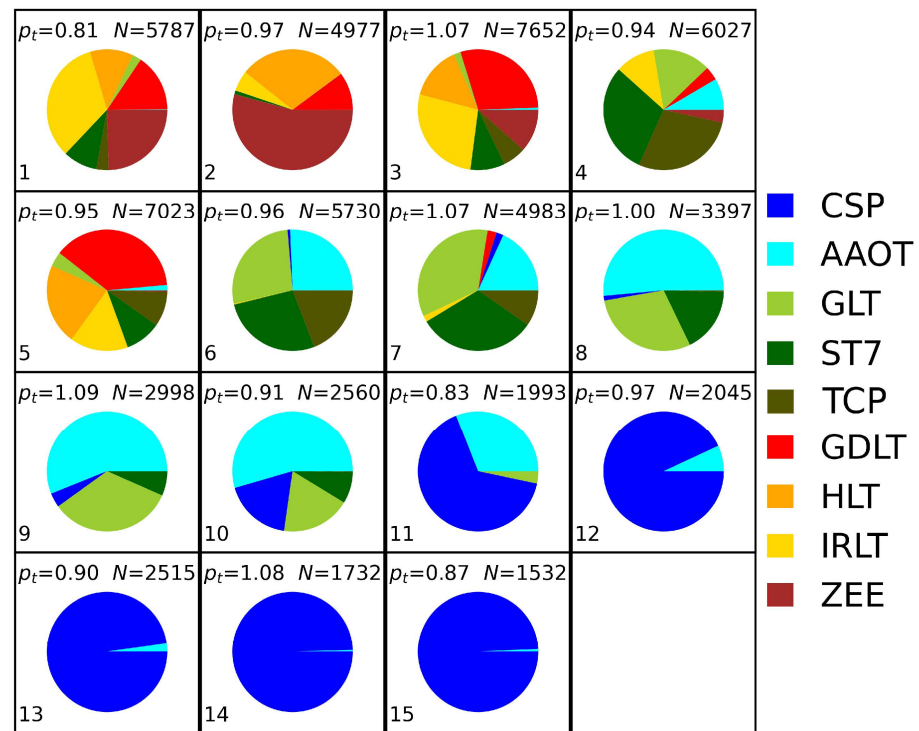


Figure 5. AERONET-OC sites relative contribution to the 15 clusters. N is the number of spectra in each cluster and p_t the average total membership for the cluster, while the number on the bottom-left corner indicates the cluster.

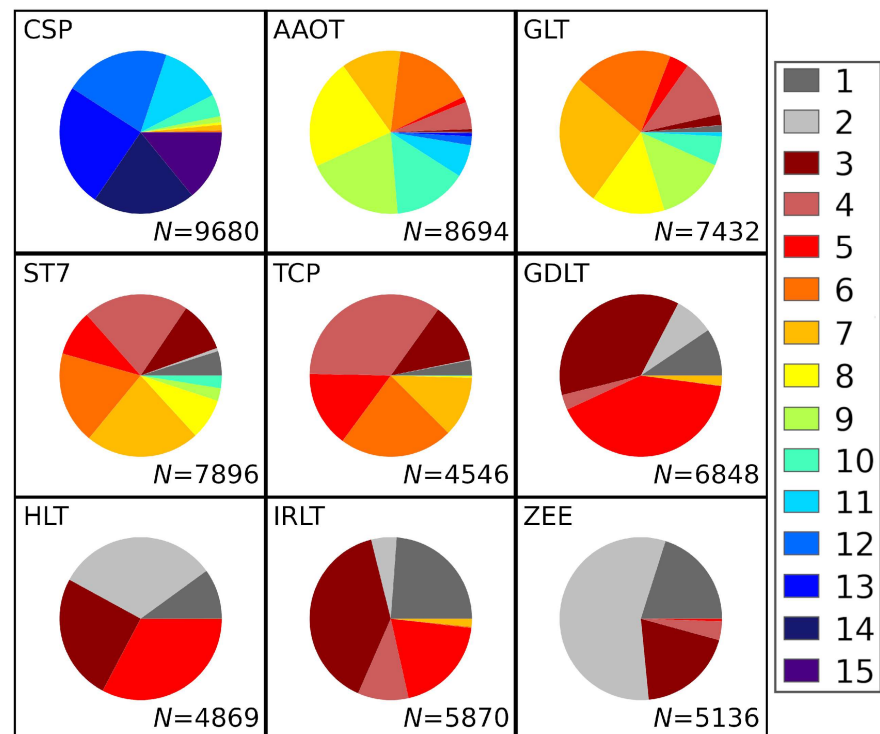


Figure 6. Cluster distribution among AERONET-OC sites. N is the number of spectra at each site.

3.3. Classification of European Sea Waters

The various ‘OLCI-XX’ sets were used to classify the OLCI 2022 time series. In practice, $nR_{RS}(\lambda)$ of any single bin for any single day was classified with all the ‘OLCI-XX’ sets. The maximum class membership was calculated for each site-specific set of classes, and the site

of the set showing the highest class membership value was assigned as most representative for that bin on that day. Class membership was preferred to total membership to avoid that the number of total classes at each site could affect the results. The most frequent site across the year was thus assigned to the bin. Figure 7 shows the most frequent site assigned to OLCI bins together with an annual mean p_t over Europe and geographically extends published validation results based on the European AERONET-OC data.

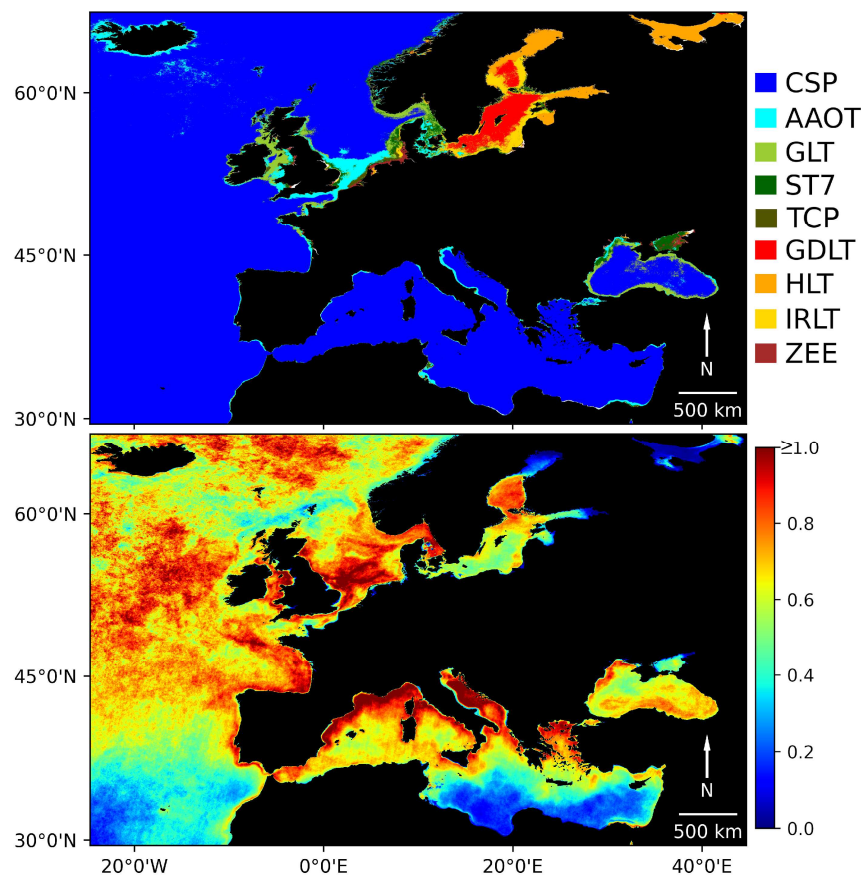


Figure 7. (Top) Most frequently assigned site in European seas in 2022 (S3A and S3B). (Bottom) Mean total membership values in 2022. Black pixels represent no data pixels.

Being representative of Case 1 waters, the CSP site is of course predominant, dominating in the open ocean and seas. However, membership values are quite low in the southern part of the Atlantic and of the Mediterranean Sea. AAOT is instead quite often selected along the Mediterranean and Atlantic coasts, but also in the English Channel, in the North Sea between England and Denmark and along North-West Danish coasts. Medium total membership values (generally between 0.3 and 0.6) are seen for the very coastal area of the Adriatic Sea, where the AAOT site is also selected, with the exception of the Northern Adriatic, where this site is actually located and high memberships are observed. Along the Northern Sea shores from Belgium to Denmark, the ZEE and TCP sites are usually selected, replaced by IRLT and ST7 as moving away from the coast. The three Baltic sites are dominant only in the Baltic Sea, with GDLT prominent in the Baltic Proper. However, moving northward in the Gulf of Bothnia and in the end of the Gulf of Finland (and in the White Sea), the membership values drastically fall. Finally, in the Black Sea, away from the coasts where GLT and ST7 dominate (together with AAOT), the CSP site is more frequently selected, associated with a high value of total membership. Interestingly, ZEE-like waters are also detected in some areas of the Azov Sea, which is indeed characterized by highly turbid waters.

The ‘OLCI-all’ set was also used to classify the OLCI 2022 time series, with the results shown in Figure 8. Clear-water classes dominate in the Mediterranean Sea and in the Atlantic Ocean, where, however, various classes from 10 to 15 are shown. Class 10 is also predominant in the Norwegian Sea, just moving away from the coasts, whereas class 11 also characterizes the North Adriatic and the Mediterranean coasts (partially), the Gibraltar strait, the Alboran Sea, and the Atlantic Ocean close to the Iberian Peninsula. Classes 1 and 2 dominate in the southern coastal area of the North and Baltic Seas, the coastal area of the Azov Sea, and a large part of the British coasts. Moving away from those areas, classes 3 and 4 dominate. Class 5 is shown almost only in the Baltic and White Seas. Class 6, typical of the GLT area, dominates in the English Channel (together with class 8), the Adriatic coastal area, and in the southern North Sea, from England to Denmark. Class 7, typical of the North-West Black Sea, is also encountered in the North Sea, not too far away from the coast. Class 9 is mostly shown in the Black Sea and more rarely along the Adriatic, Tyrrhenian, and other Mediterranean coasts. Considering S3A and S3B separately, class distributions are very similar and are almost identical in the coastal areas.

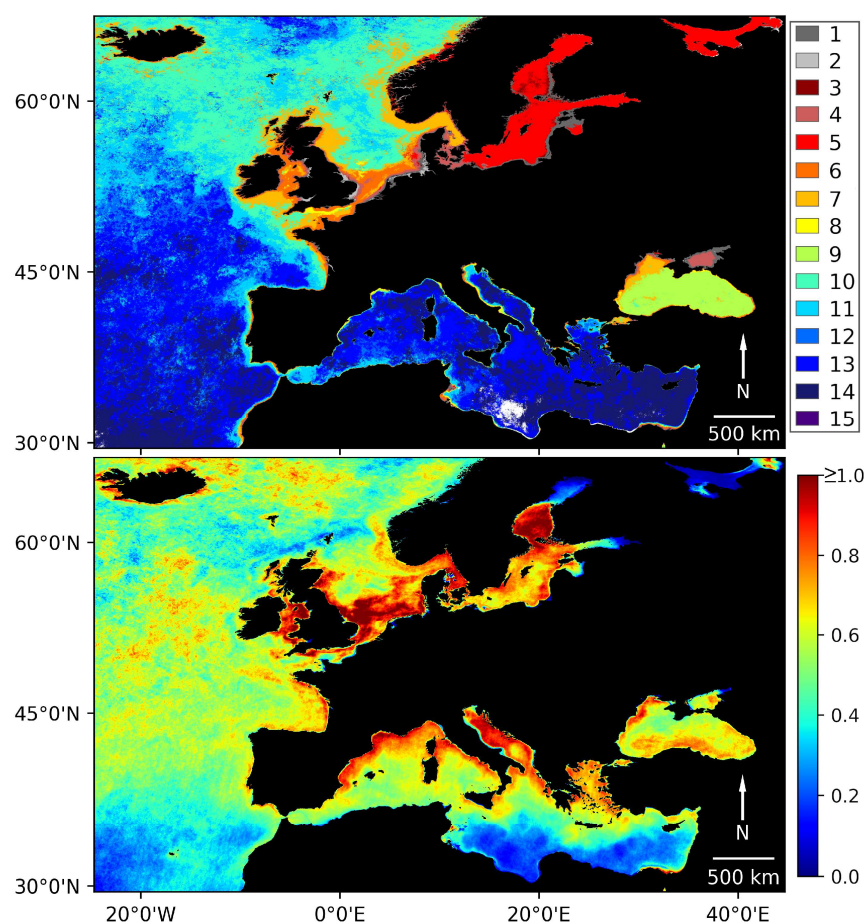


Figure 8. (Top) Most frequently assigned class (from the 15-cluster set) in European seas in 2022 (S3A and S3B). Black and white pixels represent no data and unclassified pixels, respectively. (Bottom) Mean total membership values in 2022.

3.4. Class-Specific Uncertainties and Uncertainty Distribution

The mean spectral $RMSD_u(\lambda)$ was estimated for each class of the ‘OLCI-all’ set for both S3A and S3B satellites. The choice of $RMSD_u(\lambda)$ was favored by its being free from systematic contributions, which may be different for OLCI data from S3A and S3B [6].

Figure 9 shows $RMSD_u(\lambda)$ values for all the classes. The largest values are usually reported for blue bands, with $RMSD_u(\lambda)$ decreasing monotonically with the wavelength for almost all classes. Exceptions are represented by classes 1 and 2, for which higher values

in the green and red are mostly due to the contribution by the ZEE-site turbid waters. In general, $RMSD_u(\lambda)$ for clear-water classes tends to be relatively high in the blue and low in the red, reflecting the amplitude of $R_{RS}(\lambda)$ itself, while the opposite is observed for turbid waters. This behavior has been noticed for validation statistics obtained at CSP and at Baltic sites, respectively, (e.g., [6,12]).

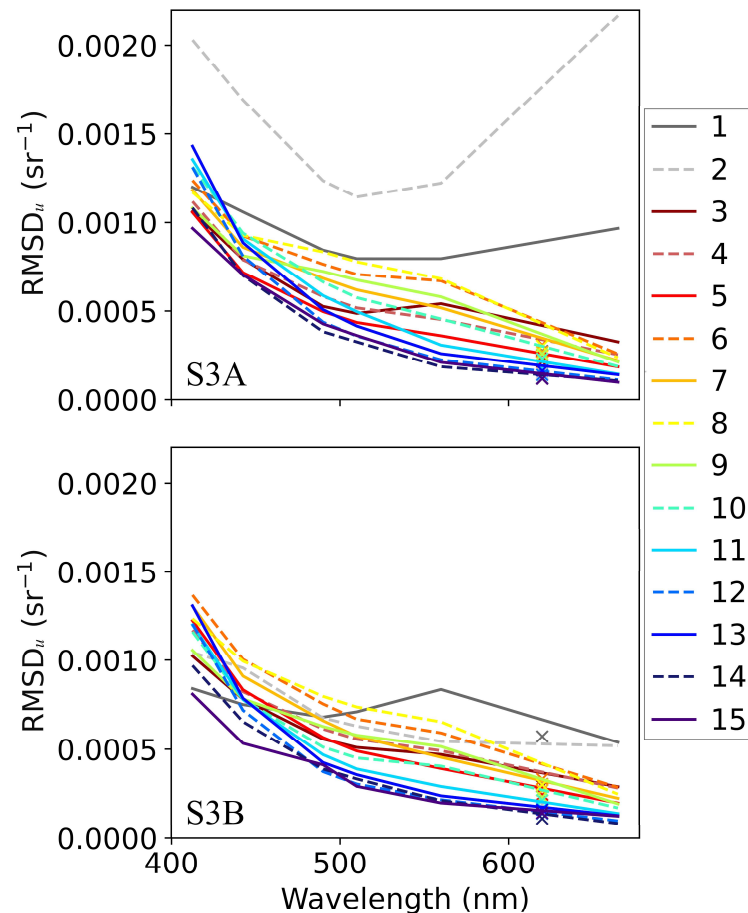


Figure 9. $RMSD_u(\lambda)$ for AERONET-OC and OLCI match-ups for (top) S3A and (bottom) S3B. Crosses indicate the values for 620 nm center-wavelengths calculated without ZEE and TCP match-up values (where $R_{RS}(620)$ is not available).

S3B (see bottom panel of Figure 9) shows equal or lower values at all classes except for classes 4 and 5 and for blue bands of class 6, whose $RMSD_u(\lambda)$ values are slightly larger than for S3A. Class 1 also shows very different values in the red, whereas class 2 shows completely different values. However, for class 2, no match-ups were available from S3B at the ZEE site. More in general, it should be considered that a very low number of match-ups (see Table 2) contributed to the definition of class 2 $RMSD_u(\lambda)$ and estimated values could not be considered robust for S3B. For these reasons, and also to avoid redundancy, results are hereafter shown only for S3A.

Applying the spectral values of $RMSD_u(\lambda)$ to the OLCI 2022 time series (according to Equation (9)) produced the results shown in Figure 10 for a few selected center-wavelengths. Unsurprisingly, the largest $RMSD_u(\lambda)$ values in the blue bands are shown in the Atlantic and in very turbid coastal waters and overall remain in a restricted range (above 0.001 sr^{-1}). From a spatial point of view, $RMSD_u(\lambda)$ are larger in the North and Baltic seas and in coastal areas in the green and in the red bands, in particular along the coasts of the North, Baltic, Black, and Northern Adriatic seas. For these wavelengths, $RMSD_u(\lambda)$ varies several-fold across the European seas. It should be noted that class statistics were not assigned when pixels were identified as novel, i.e., the average values reported were calculated accounting

only for classifiable pixels. Thus, as can be inferred from panel d of Figure 10, which shows the frequency of novelty detection in 2022, reported statistics should be considered with caution in the Gulf of Bothnia, the White Sea, the South-East Mediterranean Sea, and in the Atlantic, west of the Gibraltar strait.

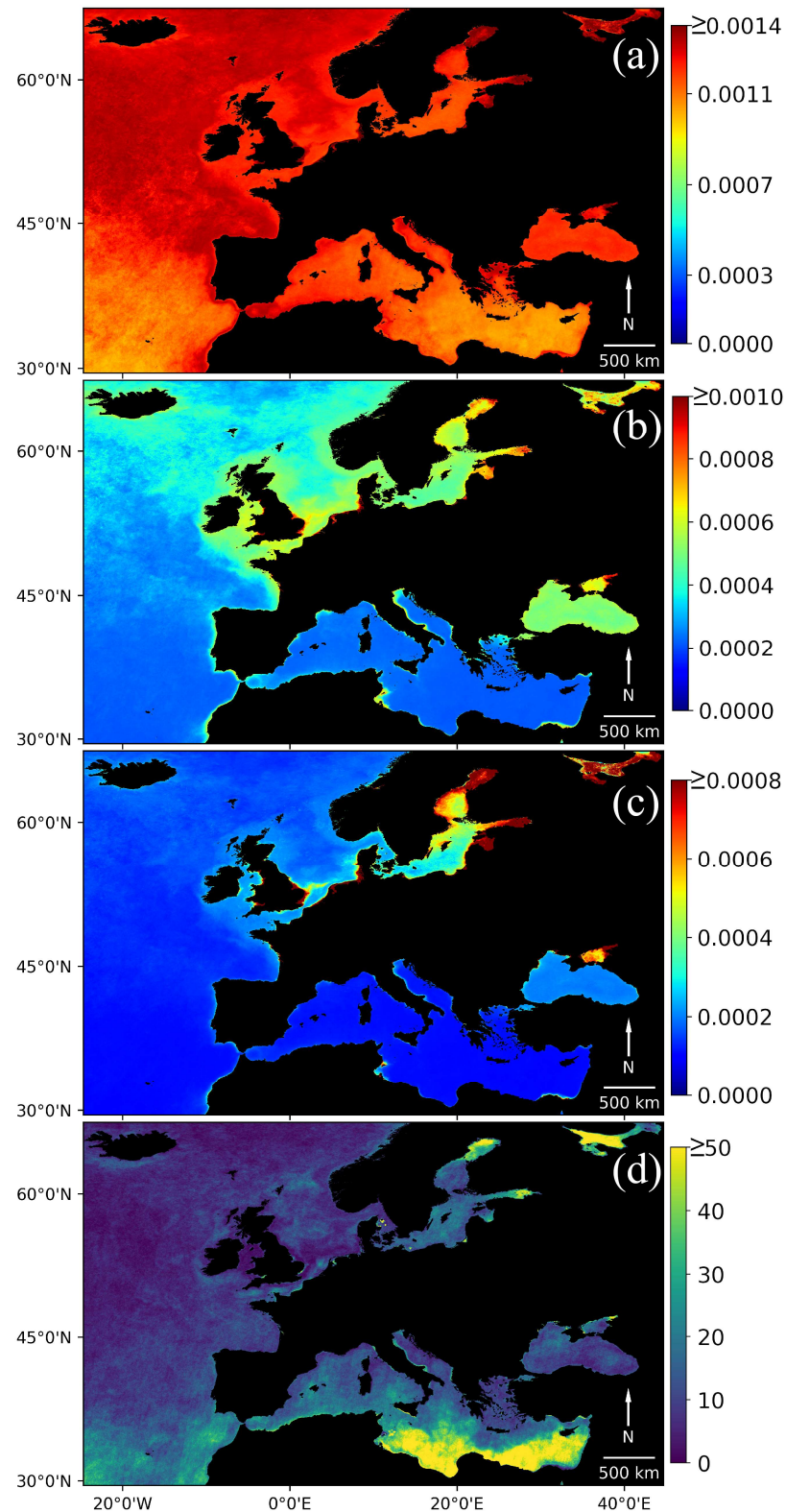


Figure 10. Average $RMSD_{II}(\lambda)$ (in sr^{-1}) at (a) 412.5 nm, (b) 560 nm, and (c) 665 nm and (d) novelty frequency map (in %) for S3A data in 2022.

Table 2. Effective match-up contributions (i.e., sum of $p(c, m)$) to each class for S3A (P_A) and S3B (P_B).

c	P_A	P_B	c	P_A	P_B
1	25.0	25.8	9	102.8	94.4
2	17.6	8.1	10	72.3	67.1
3	73.2	59.4	11	28.2	38.8
4	115.8	101.4	12	41.8	47.1
5	86.3	75.3	13	54.7	51.0
6	126.9	122.2	14	25.5	25.1
7	122.5	116.7	15	22.0	21.0
8	110.3	112.4			

3.5. Seasonal Variability

The seasonal variability of the classifiability of the European waters was also investigated. Total membership, shown in Figure 11, is generally higher in summer (some northern regions are also affected by a lack of data coverage in winter and autumn). However, the South-East Mediterranean Sea results unclassified (with p_t values close or equal to 0) in summer, whereas it shows quite a high p_t in winter time. This is not surprising considering the ultra-oligotrophic conditions characterizing this area in the late summer, leading to $R_{RS}(\lambda)$ spectra not represented by any of the AERONET-OC sites. More generally, the ultra-oligotrophic conditions of this region appear to challenge classification schemes, as already noted in [34], which might be partly explained by specific optical properties [47,48]. Conversely, the total membership is quite high in the entire Mediterranean Sea in winter, and it shows medium values along Italian coasts in winter and autumn. Also, in most parts of the Black Sea, highest total membership values are shown in autumn. It is acknowledged that the exact spatial features shown in Figure 11 might vary for different years.

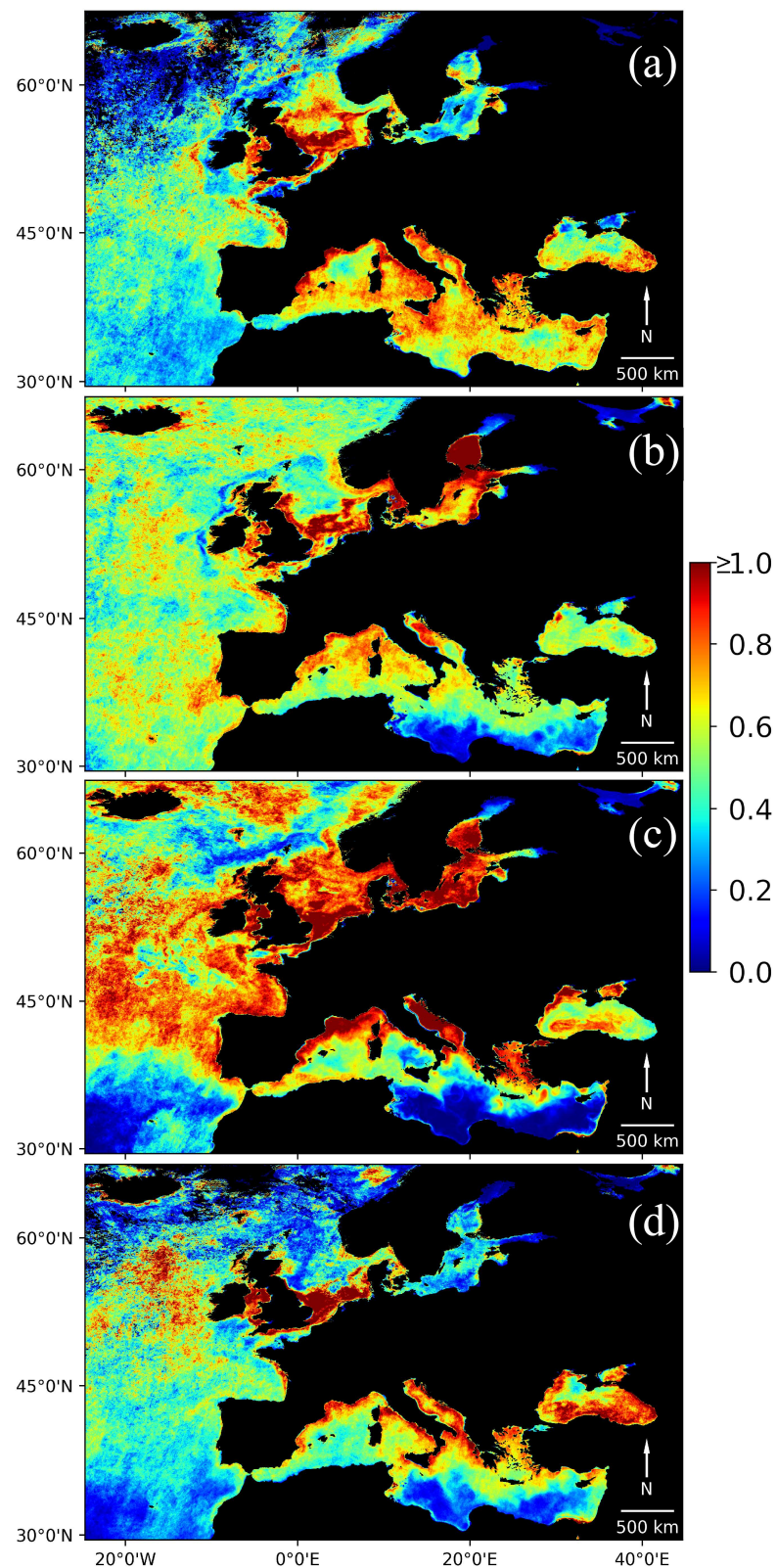


Figure 11. S3A mean total membership p_t for the various 2022 seasons: (a) winter, (b) spring, (c) summer, and (d) autumn.

4. Discussion

European sea waters were classified through a classification scheme obtained from standard Level 2 ocean color OLCI products provided by EUMETSAT (Collection 3). The

use of satellite-derived classes was also adopted in previous works, such as [25,34], in order to incorporate the whole range of variability observed spatially and seasonally in natural waters, which may be limited when using in situ observations [24]. This holds true in particular for those sites where instruments are deployed for a limited number of months each year. In this work, however, this choice was dictated not only by the fact that satellite data are those to which a classification is finally applied but also by the degraded accuracies affecting these products in optically complex waters, as reported by [6]. Their effects, in terms of potential misclassification, were confirmed by the results obtained in Section 3.2. It is, however, acknowledged that using field data to derive a set of optical classes would be an ideal choice, being independent of satellite missions and, in particular for AERONET-OC data, not being affected by clouds, glint, or low-sun elevation angle contaminations. It is also recognized that satellite-based clustering and classification results may be strongly impacted by the uncertainties affecting $R_{RS}(\lambda)$ as a result of the atmospheric correction process. The option adopted here has the advantage of maintaining coherence between data used in the clustering process and in the subsequent classification in European seas. A corollary is that the derived set of classes is only applicable for that type of data (i.e., EUMETSAT standard Ocean Color products). Eventually, more work on the issue of uncertainties with respect to classification schemes would be needed (see recommendations in [49]).

A second point of discussion is associated with the use of normalized spectra $nR_{RS}(\lambda)$ for clustering. The application of normalization to $R_{RS}(\lambda)$ values finds its justification in a number of previous works [34,35,50]. In particular, [35] reported on the advantages of normalization, which allow for reducing $R_{RS}(\lambda)$ spectra first-order variability and focusing on their spectral shape. The drawback is that spectra related to waters with different levels of clarity may be included in the same cluster. Conversely, without applying any normalization, clustering results would be influenced by a gradient in concentrations, particularly of particles [34].

Although the normalization of $R_{RS}(\lambda)$ spectra applied before data clustering should help overcoming the effect of overall over- or under-estimations in $R_{RS}(\lambda)$ values, quite good accuracy in spectral shape is also required by classification techniques but is not always granted by satellite products. Certainly, there are a number of cases when unrealistic spectral shapes are still shown (see, for example, Figure 2 in [6], where a few spectra with a spectral maximum at 400 nm are shown for CDOM-dominated sites). Aiming at reducing their effects, these spectra (about 6000 spectra over a total of more than 67,000) were excluded by the initial dataset used in the cluster analysis on the basis of expert knowledge of the optical variability observed at the various AERONET-OC sites. However, unreliable spectra could not be a priori excluded when classifying OLCI images at the continental scale. In fact, they could often result in being unclassified, classified with low membership values, or misclassified into some class not expected in their belonging regions. This can of course result in a decrease in the mean total membership values, even near the AERONET-OC sites. Unreliable spectra were not excluded when defining class uncertainties, but corresponding in situ spectra were instead used to define class and membership values (see Section 2.5). In these cases, the class assigned to the matching in situ spectrum was considered. It is acknowledged that the criteria used to exclude suspicious spectra do not assure that no unrealistic values are included at any sites. Besides unrealistic spectra, the clustering technique may have difficulty in handling spectra associated with conditions occurring infrequently (e.g., coccolithophore blooms) and, therefore, with a numerical weight, with respect to the overall data set, insufficient to generate a class. These specific conditions may deserve dedicated classes (e.g., [51]).

Class-based validation statistics do not show dramatically different spectral shapes across classes, particularly for those classes closest to each other. This is coherent with the results obtained for similar atmospheric correction processors by [11,28]. Still, match-up analysis results may be affected by different observation (Sun and observation zenith angles, SZA and OZA) or environmental (aerosol optical thickness (AOT), aerosol type, glint, etc.) conditions.

However, AOT-class mean and standard deviation values are similar between the various classes and for S3A and S3B. Looking at the satellite viewing angle, classes also show quite similar values, with few exceptions (i.e., classes 1 and 5, see Table S1 in the Supplementary Materials), still with mean values comprised between 19° and 29° . Finally, the Sun zenith angle also shows similar values, with the exception of classes from 11 to 13, for which both mean and standard deviation values are relatively high. To investigate the potential effect of these differences, class-based validation statistics were re-evaluated, limiting the analysis to match-ups satisfying the following criteria: (I) $SZA < 50^\circ$, (II) $OZA < 30^\circ$, (III) $SZA < 50^\circ$ and $OZA < 30^\circ$. The largest changes in $RMSD_u(\lambda)$ were obtained when both Sun and observation zenith angles were limited, obtaining a quite large variation in $RMSD_u(\lambda)$ at all classes, +20% on average, between -8% (at 560 nm, in class 11) to $+60\%$ (at 490 nm, in class 1). These results need to be interpreted with some caution, as the number of match-ups per class becomes uneven and fairly low in some cases when limitations to geometry angle values apply.

Similar analyses could be performed with other validation statistics. $RMSD_u(\lambda)$ was selected, as it does not include systematic contributions (biases), that could be different between S3A and S3B, and as it can be a reasonable proxy for actual uncertainties [12,15,52]. Validation statistics could be interpreted in terms of actual uncertainties, taking the uncertainties of the field data (quantified in [53,54]) into account [12,15], but this would require a larger number of match-ups across classes.

As anticipated, the choice of ISODATA parameters might also have impacted the results of clustering and thus of classification. The classification of European waters was thus repeated using alternative sets of clusters (generated with alternative ISODATA criteria) of 12 and 23 clusters. The distribution of the mean total membership is quite similar, but its absolute values are decreased in the 12-class case and increased in the 23-class one. In the first case, the variation is generally lower than 0.1, with exceptions in the Black and North Seas, in the Northern Atlantic, the English Channel, and in the AAOT site area, where differences are usually still below 0.2. This could be well justified by the disappearance of a few classes characterizing sites with optically complex waters with varying concentrations of sediments. Also, when using the 23-class set, differences are generally below 0.15, exceeding 0.2 in the Atlantic, in turbid North Sea coastal waters and in the AAOT area, due to the increased number of clear-water classes in the 23-class set with respect to the 15-class one (see Figure S3 in the Supplementary Materials). Eventually, while there is a certain degree of arbitrariness in the final number of classes adopted, the main results of this work are conserved regardless of the number of classes.

5. Conclusions

In order to investigate where the results from AERONET-OC and operational Ocean Color OLCI products match-up analyses could be extended in the European seas, different sets of classes were generated using OLCI-derived $R_{RS}(\lambda)$ spectra extracted over these sites. A cluster analysis allowed for identifying the variability in terms of optical water types associated with AERONET-OC data at the various sites and, in some cases, within each single site data. It also allowed for defining class-specific uncertainty values presented through the centered root mean squared difference $RMSD_u(\lambda)$. In general, $RMSD_u(\lambda)$ for clear-water classes tends to be relatively high in the blue center-wavelengths and low in the red ones, reflecting the amplitude of $R_{RS}(\lambda)$ itself, while the opposite is observed for turbid waters, which is in line with previous assessments (e.g., [6,12]).

The classification of OLCI time series over European seas allowed, on one hand, to identify where uncertainties estimated through AERONET-OC match-ups may be applicable and to relate the large body of literature presenting validation results based on these data to a broader geographical framework. Conversely, it also allowed to identify those (novel) areas characterized by a low level of classification, i.e., those areas scarcely represented or not represented at all by AERONET-OC data and for which AERONET-OC-derived uncertainty estimates may not be valid. These are, in particular, the southern and eastern region of the Mediterranean Sea, the Atlantic Ocean region off the African coast,

the White Sea, the Gulf of Bothnia, and part of the Gulf of Finland in the Baltic Sea. These regions are generally characterized by ultra-oligotrophic conditions (as in the case of the Eastern Mediterranean Sea) or by optical and environmental conditions which challenge atmospheric correction process (as in the case of the Gulf of Bothnia and the White Sea, characterized by high water column absorption, and thus very low reflectance values, combined with very low solar angles). A cluster analysis including all AERONET-OC sites available worldwide may be repeated to assess whether a better classifiability for these regions would be possible with a different class distribution. Still, large membership values suggest the applicability of these uncertainty estimates to a large part of the European marine waters, including the Atlantic Ocean and the North Sea and large parts of the Baltic, Mediterranean, and Black seas. Even though not ideal, the current set of AERONET-OC sites operated in Europe therefore covers a large range of the optical variability found in European seas. Additionally, a new site has recently been deployed in the Atlantic Ocean, in the Canary Islands (PLOCAN_Tower). Its data may provide useful observations to fill some gaps for oligotrophic waters.

Supplementary Materials: The following supporting information can be downloaded at: <https://www.mdpi.com/article/10.3390/rs16101793/s1>. Mean spectral $R_{RS}(\lambda)$ values at the various AERONET-OC sites from in situ and OLCI data; mean and standard deviation values of the clusters identified by ISODATA with alternative parametrizations; class-based statistics of Sun and viewing zenith angles and aerosol optical thickness for S3A and S3B match-ups.

Author Contributions: Conceptualization, I.C. and F.M.; Methodology, I.C. and F.M.; Software, I.C. and F.M.; Formal analysis, I.C. and F.M.; Investigation, I.C. and F.M.; Writing—original draft, I.C. and F.M.; Writing—review & editing, I.C. and F.M.; Visualization, I.C.; Supervision, F.M.; Project administration, F.M.; Funding acquisition, F.M. All authors have read and agreed to the published version of the manuscript.

Funding: This work benefitted from support from the Joint Research Centre through the FOLEO project. The support provided by DG DEFIS, i.e., the European Commission Directorate General for Defence Industry and Space, and the Copernicus Programme is also gratefully acknowledged.

Data Availability Statement: Data used in this work are from publicly available datasets. These datasets are available at https://aeronet.gsfc.nasa.gov/new_web/ocean_color.html and <https://data.eumetsat.int/data/map/EO:EUM:DAT:0408>.

Acknowledgments: The authors would like to thank the AERONET-OC PIs Giuseppe Zibordi, Dimitry Van der Zande, Marco Talone, and Barbara Bulgarelli for their effort in establishing and maintaining the European sites included in this study. They also thank EUMETSAT for granting access to Sentinel-3 OLCI-A and OLCI-B data. They finally thank the three anonymous reviewers for their precious contribution.

Conflicts of Interest: The authors declare no conflicts of interest.

References

1. Zibordi, G.; Mélin, F.; Berthon, J.-F.; Holben, B.; Slutsker, I.; Giles, D.; D'Alimonte, D.; Vandemark, D.; Feng, H.; Schuster, G.; et al. AERONET-OC: A Network for the Validation of Ocean Color Primary Products. *J. Atmos. Ocean. Technol.* **2009**, *26*, 1634–1651. [[CrossRef](#)]
2. Zibordi, G.; Holben, B.N.; Talone, M.; D'Alimonte, D.; Slutsker, I.; Giles, D.M.; Sorokin, M.G.; D'Alimonte, D.; Slutsker, I.; Giles, D.M.; et al. Advances in the Ocean Color Component of the Aerosol Robotic Network (AERONET-OC). *J. Atmos. Ocean. Technol.* **2021**, *38*, 725–746. [[CrossRef](#)]
3. Van der Zande, D.; Vanhellefont, Q.; De Keukelaere, L.; Knaeps, E.; Ruddick, K. Validation of Landsat-8/OLI for Ocean Colour Applications with AERONET-OC Sites in Belgian Coastal Waters. In Proceedings of the Ocean Optics Conference, Victoria, BC, Canada, 23–28 October 2016.
4. Vanhellefont, Q.; Ruddick, K. Atmospheric Correction of Metre-Scale Optical Satellite Data for Inland and Coastal Water Applications. *Remote Sens. Environ.* **2018**, *216*, 586–597. [[CrossRef](#)]
5. Zibordi, G.; Berthon, J.F.; Mélin, F.; D'Alimonte, D.; Kaitala, S. Validation of Satellite Ocean Color Primary Products at Optically Complex Coastal Sites: Northern Adriatic Sea, Northern Baltic Proper and Gulf of Finland. *Remote Sens. Environ.* **2009**, *113*, 2574–2591. [[CrossRef](#)]

6. Zibordi, G.; Kwiatkowska, E.; Mélin, F.; Talone, M.; Cazzaniga, I.; Dessailly, D.; Gossn, J.I. Assessment of OLCI-A and OLCI-B Radiometric Data Products across European Seas. *Remote Sens. Environ.* **2022**, *272*, 112911. [[CrossRef](#)]
7. Mélin, F.; Zibordi, G.; Berthon, J.-F.; Bailey, S.; Franz, B.; Voss, K.; Flora, S.; Grant, M. Assessment of MERIS Reflectance Data as Processed with SeaDAS over the European Seas. *Opt. Express* **2011**, *19*, 25657. [[CrossRef](#)] [[PubMed](#)]
8. Pahlevan, N.; Mangin, A.; Balasubramanian, S.V.; Smith, B.; Alikas, K.; Arai, K.; Barbosa, C.; Bélanger, S.; Binding, C.; Bresciani, M.; et al. ACIX-Aqua: A Global Assessment of Atmospheric Correction Methods for Landsat-8 and Sentinel-2 over Lakes, Rivers, and Coastal Waters. *Remote Sens. Environ.* **2021**, *258*, 112366. [[CrossRef](#)]
9. Mélin, F.; Zibordi, G.; Berthon, J.-F. Uncertainties in Remote Sensing Reflectance From MODIS-Terra. *IEEE Geosci. Remote Sens. Lett.* **2012**, *9*, 432–436. [[CrossRef](#)]
10. Mélin, F.; Sclep, G.; Jackson, T.; Sathyendranath, S. Uncertainty Estimates of Remote Sensing Reflectance Derived from Comparison of Ocean Color Satellite Data Sets. *Remote Sens. Environ.* **2016**, *177*, 107–124. [[CrossRef](#)]
11. Mélin, F.; Franz, B.A. Assessment of Satellite Ocean Colour Radiometry and Derived Geophysical Products. In *Optical Radiometry for Ocean Climate Measurements*; Zibordi, G., Donlon, C.J., Parr, A.C., Eds.; Experimental Methods in the Physical Sciences; Academic Press: Cambridge, MA, USA, 2014; Volume 47, pp. 609–638.
12. Mélin, F. Validation of Ocean Color Remote Sensing Reflectance Data: Analysis of Results at European Coastal Sites. *Remote Sens. Environ.* **2022**, *280*, 113153. [[CrossRef](#)]
13. Mélin, F.; Zibordi, G.; Carlund, T.; Holben, B.N.; Stefan, S. Validation of SeaWiFS and MODIS Aqua/Terra Aerosol Products in Coastal Regions of European Marginal Seas. *Oceanologia* **2013**, *55*, 27–51. [[CrossRef](#)]
14. Zibordi, G.; Mélin, F.; Berthon, J.-F. A Regional Assessment of OLCI Data Products. *IEEE Geosci. Remote Sens. Lett.* **2018**, *15*, 1490–1494. [[CrossRef](#)]
15. Mélin, F. From Validation Statistics to Uncertainty Estimates: Application to VIIRS Ocean Color Radiometric Products at European Coastal Locations. *Front. Mar. Sci.* **2021**, *8*, 790948. [[CrossRef](#)]
16. Cazzaniga, I.; Zibordi, G.; Melin, F.; Kwiatkowska, E.; Talone, M.; Dessailly, D.; Gossn, J.I.; Muller, D. Evaluation of OLCI Neural Network Radiometric Water Products. *IEEE Geosci. Remote Sens. Lett.* **2022**, *19*, 1–5. [[CrossRef](#)]
17. Tilstone, G.; Dall’Omo, G.; Hieronymi, M.; Ruddick, K.; Beck, M.; Ligi, M.; Costa, M.; D’Alimonte, D.; Vellucci, V.; Vansteenkoven, D.; et al. Field Intercomparison of Radiometer Measurements for Ocean Colour Validation. *Remote Sens.* **2020**, *12*, 1587. [[CrossRef](#)]
18. Steinmetz, F.; Ramon, D. Sentinel-2 MSI and Sentinel-3 OLCI Consistent Ocean Colour Products Using POLYMER. In *Proceedings of the Remote Sensing of the Open and Coastal Ocean and Inland Waters, Honolulu, HI, USA, 24–25 September 2018*; Frouin, R.J., Murakami, H., Eds.; SPIE: Bellingham, WA, USA, 2018; p. 13.
19. Gilerson, A.; Herrera-Estrella, E.; Agagiate, J.; Foster, R.; Gossn, J.I.; Dessailly, D.; Kwiatkowska, E. Determining the Primary Sources of Uncertainty in the Retrieval of Marine Remote Sensing Reflectance from Satellite Ocean Color Sensors II. Sentinel 3 OLCI Sensors. *Front. Remote Sens.* **2023**, *4*, 1146110. [[CrossRef](#)]
20. Liu, H.; He, X.; Li, Q.; Hu, X.; Ishizaka, J.; Kratzer, S.; Yang, C.; Shi, T.; Hu, S.; Zhou, Q.; et al. Evaluation of Ocean Color Atmospheric Correction Methods for Sentinel-3 OLCI Using Global Automatic In Situ Observations. *IEEE Trans. Geosci. Remote Sens.* **2022**, *60*, 1–19. [[CrossRef](#)]
21. Kyriliuk, D.; Kratzer, S. Evaluation of Sentinel-3A OLCI Products Derived Using the Case-2 Regional CoastColour Processor over the Baltic Sea. *Sensors* **2019**, *19*, 3609. [[CrossRef](#)]
22. Moore, T.S.; Campbell, J.W.; Dowell, M.D. A Class-Based Approach to Characterizing and Mapping the Uncertainty of the MODIS Ocean Chlorophyll Product. *Remote Sens. Environ.* **2009**, *113*, 2424–2430. [[CrossRef](#)]
23. Sathyendranath, S.; Brewin, R.J.W.; Brockmann, C.; Brotas, V.; Calton, B.; Chuprin, A.; Cipollini, P.; Couto, A.B.; Dingle, J.; Doerffer, R.; et al. An Ocean-Colour Time Series for Use in Climate Studies: The Experience of the Ocean-Colour Climate Change Initiative (OC-CCI). *Sensors* **2019**, *19*, 4285. [[CrossRef](#)]
24. IOCCG. *Uncertainties in Ocean Colour Remote Sensing*. IOCCG Report Series, Number 18; Mélin, F., Ed.; International Ocean Colour Coordinating Group: Dartmouth, NS, Canada, 2019.
25. Jackson, T.; Sathyendranath, S.; Mélin, F. An Improved Optical Classification Scheme for the Ocean Colour Essential Climate Variable and Its Applications. *Remote Sens. Environ.* **2017**, *203*, 152–161. [[CrossRef](#)]
26. Liu, X.; Steele, C.; Simis, S.; Warren, M.; Tyler, A.; Spyrakos, E.; Selmes, N.; Hunter, P. Retrieval of Chlorophyll-a Concentration and Associated Product Uncertainty in Optically Diverse Lakes and Reservoirs. *Remote Sens. Environ.* **2021**, *267*, 112710. [[CrossRef](#)]
27. Moore, T.S.; Campbell, J.W.; Feng, H. Characterizing the Uncertainties in Spectral Remote Sensing Reflectance for SeaWiFS and MODIS-Aqua Based on Global In Situ Matchup Data Sets. *Remote Sens. Environ.* **2015**, *159*, 14–27. [[CrossRef](#)]
28. Goyens, C.; Jamet, C.; Schroeder, T. Evaluation of Four Atmospheric Correction Algorithms for MODIS-Aqua Images over Contrasted Coastal Waters. *Remote Sens. Environ.* **2013**, *131*, 63–75. [[CrossRef](#)]
29. Hieronymi, M.; Bi, S.; Müller, D.; Schütt, E.M.; Behr, D.; Brockmann, C.; Lebreton, C.; Steinmetz, F.; Stelzer, K.; Vanhellefont, Q. Ocean Color Atmospheric Correction Methods in View of Usability for Different Optical Water Types. *Front. Mar. Sci.* **2023**, *10*, 1129876. [[CrossRef](#)]
30. Mélin, F.; Sclep, G. Band Shifting for Ocean Color Multi-Spectral Reflectance Data. *Opt. Express* **2015**, *23*, 2262–2279. [[CrossRef](#)] [[PubMed](#)]
31. Salem, S.I.; Higa, H.; Ishizaka, J.; Pahlevan, N.; Oki, K. Spectral Band-Shifting of Multispectral Remote-Sensing Reflectance Products: Insights for Matchup and Cross-Mission Consistency Assessments. *Remote Sens. Environ.* **2023**, *299*, 113846. [[CrossRef](#)]

32. Morel, A.; Antoine, D.; Gentili, B. Bidirectional Reflectance of Oceanic Waters: Accounting for Raman Emission and Varying Particle Scattering Phase Function. *Appl. Opt.* **2002**, *41*, 6289–6306. [[CrossRef](#)]
33. Thuillier, G.; Hersé, M.; Labs, D.; Foujols, T.; Peetermans, W.; Gillotay, D.; Simon, P.C.; Mandel, H. The Solar Spectral Irradiance from 200 to 2400 Nm as Measured by the SOLSPEC Spectrometer from the Atlas and Eureka Missions. *Sol. Phys.* **2003**, *214*, 1–22. [[CrossRef](#)]
34. Mélin, F.; Vantrepotte, V. How Optically Diverse Is the Coastal Ocean? *Remote Sens. Environ.* **2015**, *160*, 235–251. [[CrossRef](#)]
35. Vantrepotte, V.; Loisel, H.; Dessailly, D.; Mériaux, X. Optical Classification of Contrasted Coastal Waters. *Remote Sens. Environ.* **2012**, *123*, 306–323. [[CrossRef](#)]
36. EUMETSAT. *Sentinel-3 OLCI L2 Report for Baseline Collection OL_L2M_003*; EUM/RSP/REP/21/1211386; EUMETSAT: Darmstadt, Germany, 2021.
37. Memarsadeghi, N.; Mount, D.M.; Netanyahu, N.S.; Le Moigne, J. A Fast Implementation of the ISODATA Clustering Algorithm. *Int. J. Comput. Geom. Appl.* **2007**, *17*, 71–103. [[CrossRef](#)]
38. Moore, T.S.; Campbell, J.W.; Feng, H. A Fuzzy Logic Classification Scheme for Selecting and Blending Satellite Ocean Color Algorithms. *IEEE Trans. Geosci. Remote Sens.* **2001**, *39*, 1764–1776. [[CrossRef](#)]
39. Mélin, F.; Vantrepotte, V.; Clerici, M.; D’Alimonte, D.; Zibordi, G.; Berthon, J.-F.; Canuti, E. Multi-Sensor Satellite Time Series of Optical Properties and Chlorophyll-a Concentration in the Adriatic Sea. *Prog. Oceanogr.* **2011**, *91*, 229–244. [[CrossRef](#)]
40. D’Alimonte, D.; Melin, F.; Zibordi, G.; Berthon, J.-F. Use of the Novelty Detection Technique to Identify the Range of Applicability of Empirical Ocean Color Algorithms. *IEEE Trans. Geosci. Remote Sens.* **2003**, *41*, 2833–2843. [[CrossRef](#)]
41. Shaun Turney Chi-Square (X2) Table. Available online: <https://www.scribbr.com/statistics/chi-square-distribution-table/> (accessed on 31 October 2023).
42. Press, W.H.; Teukolsky, S.A.; Vetterling, W.T.; Flannery, B.P. *Numerical Recipes in C: The Art of Scientific Computing*, 2nd ed.; Cambridge University Press: Cambridge, UK, 1992.
43. Berthon, J.-F. *SeaWiFS Postlaunch Technical Report Series: Part 2, Data Analysis; Coastal Atmosphere and Sea Time Series (CoASTS)*; Goddard Space Flight Center: Greenbelt, MD, USA, 2002; Volume 20.
44. Güttler, F.N.; Niculescu, S.; Gohin, F. Turbidity Retrieval and Monitoring of Danube Delta Waters Using Multi-Sensor Optical Remote Sensing Data: An Integrated View from the Delta Plain Lakes to the Western–Northwestern Black Sea Coastal Zone. *Remote Sens. Environ.* **2013**, *132*, 86–101. [[CrossRef](#)]
45. Groom, S.B.; Holligan, P.M. Remote Sensing of Coccolithophore Blooms. *Adv. Sp. Res.* **1987**, *7*, 73–78. [[CrossRef](#)]
46. Cazzaniga, I.; Zibordi, G.; Mélin, F. Spectral Variations of the Remote Sensing Reflectance during Coccolithophore Blooms in the Western Black Sea. *Remote Sens. Environ.* **2021**, *264*, 112607. [[CrossRef](#)]
47. Claustre, H.; Morel, A.; Hooker, S.B.; Babin, M.; Antoine, D.; Oubelkheir, K.; Bricaud, A.; Leblanc, K.; Quéguiner, B.; Maritorena, S. Is Desert Dust Making Oligotrophic Waters Greener? *Geophys. Res. Lett.* **2002**, *29*, 104–107. [[CrossRef](#)]
48. Morel, A.; Gentili, B. The Dissolved Yellow Substance and the Shades of Blue in the Mediterranean Sea. *Biogeosciences* **2009**, *6*, 2625–2636. [[CrossRef](#)]
49. BPIM-WMO. *Metrology for Climate Action; Report BIPM 2023/03*, WMO-IOM, 142; WMO, BIPM: Geneva, Switzerland, 2023.
50. Bi, S.; Li, Y.; Xu, J.; Liu, G.; Song, K.; Mu, M.; Lyu, H.; Miao, S.; Xu, J. Optical Classification of Inland Waters Based on an Improved Fuzzy C-Means Method. *Opt. Express* **2019**, *27*, 34838. [[CrossRef](#)] [[PubMed](#)]
51. Moore, T.S.; Dowell, M.D.; Franz, B.A. Detection of Coccolithophore Blooms in Ocean Color Satellite Imagery: A Generalized Approach for Use with Multiple Sensors. *Remote Sens. Environ.* **2012**, *117*, 249–263. [[CrossRef](#)]
52. Mélin, F.; Cazzaniga, I.; Sciuto, P. Verification of Uncertainty Estimates of Autonomous Field Measurements of Marine Reflectance Using Simultaneous Observations. *Front. Remote Sens.* **2024**, *4*, 1295855. [[CrossRef](#)]
53. Cazzaniga, I.; Zibordi, G. AERONET-OC LWN Uncertainties: Revisited. *J. Atmos. Ocean. Technol.* **2023**, *40*, 411–425. [[CrossRef](#)]
54. Gergely, M.; Zibordi, G. Assessment of AERONET-OC LWN Uncertainties. *Metrologia* **2014**, *51*, 40–47. [[CrossRef](#)]

Disclaimer/Publisher’s Note: The statements, opinions and data contained in all publications are solely those of the individual author(s) and contributor(s) and not of MDPI and/or the editor(s). MDPI and/or the editor(s) disclaim responsibility for any injury to people or property resulting from any ideas, methods, instructions or products referred to in the content.